Touchless Potential Sensing of Complex Differentially-Charged Shapes Using Secondary Electrons

Álvaro Romero-Calvo*, Julian Hammerl†, and Hanspeter Schaub ‡
Department of Aerospace Engineering Sciences, University of Colorado Boulder, CO, United States.

The secondary electron method has been recently proposed to touchlessly sense the electrostatic potential of non-cooperative objects in geosynchronous equatorial orbits and deep space. This process relies on the detection of secondaries generated at the target surface, that is irradiated by an electron beam. Although the concept has been demonstrated with basic geometries, the electric field around a complex body leads to a highly inhomogeneous distribution of secondary electrons that determines the performance of the system. This paper employs vacuum chamber experiments and particle tracing simulations to investigate the detectability of the secondary electron flux generated over a spacecraft-like electrode assembly. The differential charging scenario, in which the assembly is charged to multiple potentials, is also studied. A three-dimensional particle tracing framework that implements the coupled electron beam propagation and secondary electron generation processes is introduced and validated, showing its utility as a diagnostic tool. The spacecraft shape, potential distribution, and electron beam intersection define the detectability of the target, which is limited to well-defined spatial regions where the potentials are measured with high accuracy. The analysis provides theoretical and technical insight into the development of future electron-based remote potential sensing technologies.

I. Introduction

The use of secondary electrons [1] and x-rays [2, 3] has been recently proposed to touchlessly sense the electrostatic potential of non-cooperative objects in Geosynchronous Equatorial Orbit (GEO) and deep space. These approaches, illustrated in Fig. 1, make use of a positively charged servicing craft that directs a high-energy electron beam at the object of interest so that low-energy secondary electrons and x-rays are emitted from the surface. The secondary electron flux is accelerated toward the servicing craft and arrives with an energy equal to the potential difference between the two bodies. The servicing craft measures the electron and photon energy spectrum and, knowing its own potential, infers that of the target [4]. Several novel applications are enable by this approach, including those dealing with the electrostatic detumbling [5] and reorbiting [6–9] of debris, Coulomb formations [10], virtual structures [11], electrostatic inflation [12], and the mitigation of arcing during rendezvous, docking, and proximity operations [13].

The validation of these touchless electrostatic potential sensing methods has been addressed in previous works with flat plates, which simplify experimental procedures and ease data interpretation [1, 3, 14]. However, a flat surface is not representative of a standard spacecraft, whose complex geometry leads to a highly inhomogeneous electric field that determines the trajectories of low-energy particles [15–18]. A recent work exemplifies the importance of this effect by making use of two-dimensional shape primitives in vacuum chamber and numerical experiments, showing how concave geometries and internal corners focus the flux of secondary electrons, while convex surfaces and external corners have the opposite effect [19]. The detectability of secondary electrons at a servicing spacecraft is thus determined by the target's geometry and relative position [19] and the interaction with the electron beam [20]. The problem is further complicated when differential charging (i.e. multiple potentials) is considered. Although modern design best practices recommend all exterior surfaces to be connected to a common ground to prevent arcing events [21], numerous spacecraft are known to have suffered from differential charging in the past [22–25]. The presence of multiple potentials and deep dielectric charging further complicates the remote sensing process. On one hand, electrons are steered in different

*Graduate Research Assistant, Department of Aerospace Engineering Sciences, University of Colorado Boulder, CO, United States; alvaro.romerocalvo@colorado.edu. Student member AIAA.

†Graduate Research Assistant, Department of Aerospace Engineering Sciences, University of Colorado Boulder, CO, United States; julian.hammerl@colorado.edu. Student member AIAA.

‡Professor, Glenn L. Murphy Chair in Engineering, Ann and H.J. Smead Aerospace Engineering Sciences; hanspeter.schaub@colorado.edu. AIAA Fellow.

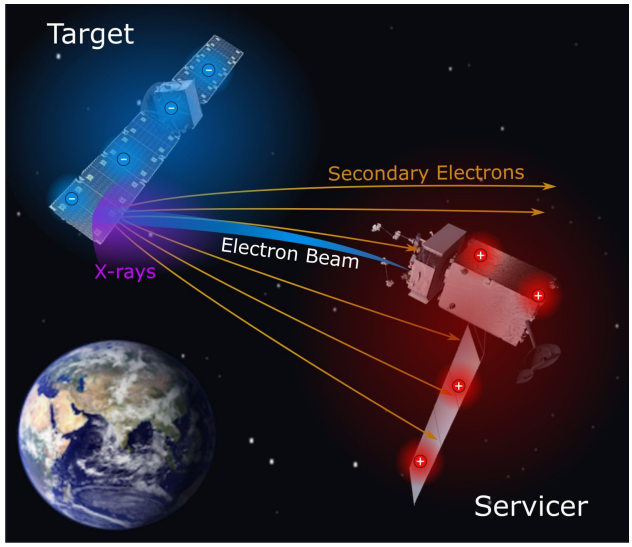

Fig. 1 Conceptual representation of the secondary electrons and x-ray-based electrostatic potential measurement processes

directions with respect to the uniform potential scenario. On the other, their observability may be severely compromised due to the generation of potential traps [19, 26].

This paper addresses the detectability of spacecraft potentials using the secondary electron method. Its primary goal is to identify the geometrical configurations for which the flux of secondaries is observable, and its magnitude. A second goal is to develop and validate a particle tracing simulation framework that enables higher fidelity simulations of the sensing process. Previously unexplored mechanisms, like the coupling between electron beam propagation and secondary electron generation, are addressed. Moreover, the effects of differential charging on a complex space-like geometry are studied for the first time. Vacuum chamber experiments are carried out at the Electrostatic Charging Laboratory for Interactions between Plasma and Spacecraft (ECLIPS) simulation facility [27] to support the study. The expansion from two to three dimensions is achieved by making use of SIMION, a popular particle tracing simulator used in the design of ion optics [28] which becomes particularly appropriate for space applications where space charge effects remain negligible. The SIMION-based model is introduced in Sec. II, and the experimental procedure is described in Sec. III. Key results and design guidelines relevant for future spacecraft applications are finally discussed in Sec. IV.

II. Particle Tracing Model

The touchless electrostatic potential sensing model here introduced is built in SIMION by means of user-defined functions programmed in Lua language. Although different particle tracing suites could be employed for this task, SIMION eases geometrical calculations and implements a solid tool set that speeds up the development process.

A. Electrostatic framework

The trajectory of each charged particle is computed in SIMION from Newton's second law

$$\frac{\mathrm{d}\boldsymbol{v}}{\mathrm{d}t} = \frac{q}{m}\boldsymbol{E}, \tag{1}$$

where $\boldsymbol{v}$, q, and m are respectively the particle velocity, charge, and mass, $\boldsymbol{E}$ is the electric field, and t is the time. Relativistic corrections are implemented when Lorentz's factor $\gamma = \sqrt{1 - v^2/c^2}$ exceeds 10^{-10}, with c being the speed of light. The electric field is derived from the electrostatic potential V as

$$\boldsymbol{E} = \nabla V, \tag{2}$$

while V is computed by solving Laplace's equation

$$\nabla^2 V = 0 \tag{3}$$

in the simulation domain. A regular Cartesian mesh is employed with the boundary conditions being determined by the predefined potentials of each electrode (Dirichlet) or by the zero-derivative of V (Neumann). The potential of the electrodes, named *potential arrays* in SIMION, can be adjusted individually by taking advantage of the additive property of the Laplace equation. The overall potential is then computed as the superposition of each solution, enabling faster simulations.

Equation 1 does not include the magnetic Lorentz force term. The geomagnetic field in GEO orbit is ~100 nT, resulting in gyroradii of 100-3000 m for electron energies from 10 to 10^4 eV. Although weak, this effect can slightly deviate the secondary electrons and should be implemented in future works. In the case of application described in Sec.III, however, the geomagnetic field is almost perfectly aligned with the electron velocities (specifically, with the electron beam), the gyroradius is several times larger than the characteristic length of the experiment, and the electric force is one order of magnitude larger than the magnetic force. For these reasons, the magnetic contribution has been neglected.

It is important to note that SIMION, by default, does not solve Poisson's equation to account for space-charge effects. This implies that the electrostatic environment is fully determined by the potential arrays, whose solution is computed before each simulation, and that the magneto-electrostatic interaction between particles is not considered. Electron beams, however, can include approximate beam repulsion models. Further details on the implications of this assumption in spacecraft charging scenarios can be found in Sec. II.C.

B. Secondary Electron Emission

When a sufficiently energetic primary electron impacts a surface, part of its energy is shared with neighboring particles, leading to the release of secondary electrons [26]. This effect is not included by default in SIMION and should be properly modeled to enable the study of active spacecraft charging. User-defined Lua functions can be written to complement the standard toolset. The modeling and implementation of the secondary electron yield, primary electron impact, angular distribution, and energy distribution are subsequently described.

1. Secondary electron yield

The probability of emission of secondaries per incoming primary electron is given by the *secondary electron yield* δ. This value depends on the incidence energy E of the impinging particle in a relation that can be approximated by Sanders and Inouye yield model [29]

$$\delta(E, 0) = c\left[e^{-E/a} - e^{-E/b}\right], \tag{4}$$

where $a = 4.3E_{\max}$, $b = 0.367E_{\max}$, and $c = 1.37\delta_{\max}$. The parameters $\delta_{\max}$ and $E_{\max}$ define the maximum yield point and characterize the surface. However, these values strongly depend on the surface structure and conditions [30–32], which may be particularly unpredictable after a prolonged exposition to the GEO environment [33]. It should be noted that $\delta(E, 0)$ may be greater than 1 between the crossover points E_1 and E_2, with $E_1 < E_{\max} < E_2$. Consequently, an incoming particle may generate more than one secondary electron [26].

Once the probability of emission for a particular primary impact is known, it is necessary to compute the number of released secondaries. It seems natural to treat this event as a Poisson point process, and thus a Poisson distribution with parameter $\lambda = \delta(E)$ is implemented using Knuth's algorithm [34]. Unlike the existing SIMION examples*, where an impacting primary electron is either terminated or steered to match a yield below 1, the model here presented employs the new experimental SIMION 8.1/8.2 function `simion.experimental.add_particles()` to create an undefined number of particles from a collision event.

The incoming electron flux may also be reflected off the surface, producing backscattered electrons [26]. These particles have much higher energies than secondary electrons and are hence easy to remove from the overall energy spectrum. For that reason, their contribution is neglected in this work.

*The interested reader is referred to the `readme.html` file in the `examples/secondary` folder of SIMION 2020

2. Effect of incident primary electron angle

The emission of secondaries is also dependent on the incidence angle of primary electrons. Darlington and Cosslett propose the relation [35]

$$\delta(E,\phi) = \delta(E,0)e^{\beta_s(E)(1-cos\phi)}, \tag{5}$$

with ϕ being the primary incidence angle, $\delta(E,0)$ the secondary electron yield obtained from Eq. 4, and

$$\beta_s(E) = e^{\zeta}, \tag{6a}$$

$$\zeta = 0.2755(\xi - 1.658) - \left\{[0.2755(\xi - 1.658)]^2 + 0.0228\right\}^{1/2}, \tag{6b}$$

$$\xi = \ln(E/E_{\max}), \tag{6c}$$

empirical factors proposed by Laframboise and Kamitsuma [26].

3. Angular distribution

The angular distribution of secondary electrons follows approximately Lambert's cosine law and is nearly independent of the angle of incidence of the impinging particle [36]. The polar angle is thus computed from an uniform 0-1 random variable x through [37]

$$\theta = \frac{1}{2}\mathrm{acos}(1-2x), \tag{7}$$

while the azimuth angle follows an uniform distribution between 0° and 360°.

4. Energy distribution

The energy E_s of a secondary electron with respect to the vacuum level is of the order of a few eV and follows a characteristic distribution with a peak at one third of the work function φ of the material. The Chung-Everhart normalized probability density function (PDF)

$$f(E_s) = \frac{6\varphi^2 E_s}{(E_s+\varphi)^4} \tag{8}$$

is commonly employed to approximate this distribution [38].

The energy of a new secondary is computed in a dedicated Lua library by applying the inversion method to the cumulative distribution function (CDF) of Eq. 8, given by

$$g(E_s) = \frac{\varphi}{3(E_s+\varphi)^3} - \frac{1}{2(E_s+\varphi)^2} + \frac{1}{6\varphi^2}. \tag{9}$$

The desired E_s is obtained by entering the CDF with a value of g sampled from a uniform distribution. However, it is not possible to derive an analytical $E_s(g)$ from Eq. 9, and thus Newton's method is implemented to compute E_s for a given g. This process is implemented in Lua taking $\varphi/3$ as an initial estimate, reaching the desired energy value within few iterations with a tolerance of ±0.01 eV.

C. Space environment

Spacecraft-plasma interactions have motivated a wide variety of fundamental and applied research because of the complex physical mechanisms involved and their impact on space instrumentation. The full consideration of these phenomena requires solving the Poisson equation and the plasma density distribution, incurring in prohibitive computational costs. In contrast, the electrostatic framework described in Sec. II.A is computational efficient because it ignores space charge effects.

In the presence of charged bodies, the surrounding plasma tends to relocate under the influence of Coulomb's force following a process known as Debye screening [39]. As a consequence, the electrostatic potential is damped in a characteristic distance given by the Debye length, which in GEO orbits is nominally about 200 m [40]. The propagation of electron beams and secondary electrons in the active spacecraft charging scenario is driven by the actual electrostatic potential, but since servicer and target spacecraft are separated by tens of meters, Debye screening is expected to have a second-order impact on the detection process. In other words, the unperturbed electrostatic potential obtained by solving the Laplace equation offers a good approximation of the actual electrostatic environment for this particular problem.

Space-charge can also lead to localized phenomena that may influence the sensing process. A number of works have reported the presence of electrostatic barriers that prevent the detection of low-energy particles and the escape of secondary electrons from the spacecraft surface [41–44]. These barriers appear when "the photoelectron density at the surface of the spacecraft greatly exceeds the ambient plasma density, the spacecraft is significantly larger than the local Debye length of the photoelectrons, and the thermal electron energy is much larger than the characteristic energy of the escaping photoelectrons" [43]. The effect is important near the Sun, but becomes far less concerning for distances beyond 0.3 AU [43, 44]. In the problem addressed by this work, the target spacecraft can charge negatively up to several kV under the influence of a well-localized electron beam. The beam landing spot generates low-energy secondary electrons that can produce their own electrostatic barrier [45]. Using a spot radius of 10 cm, unit yield, and an average secondary energy of 2 eV, the number densities of secondaries near the surface range between 200 and $2 \cdot 10^5$ cm^{-3}, resulting in secondary Debye lengths between 70 and 2 cm. These rough computations indicate that well-focused high-current beams may lead to localized electrostatic barriers. Poisson solvers are needed to further explore this issue. From a practical perspective, a mild electrostatic barrier may reduce the number of secondaries escaping the surface, but should not significantly influence their trajectory. The model here presented should then offer a reasonable approximation to the problem in most cases of technical interest.

Regarding electron-plasma interactions, it should be noted that the GEO plasma is low density (0.1-1 cm^{-3}) and high-energy (up to many keV), excluding quiet days without significant solar activity where higher densities (~100 cm^{-3}) and lower energies (few tens of eV) are observed [26]. As a consequence, the mean free path is of the order of 100 AU, and the GEO space can be considered collisionless. The same occurs in a high-vacuum environment (10^{-7} Torr) like the one generated in the ECLIPS facility, where the mean free path is about 1 km. On the other hand, the detectability of incoming secondaries is not compromised by the environment because it is several orders of magnitude larger than the background plasma flux both in active and passive potential sensing scenarios [46].

Changes in temperature can also influence the work function of the surface material [47] and its secondary electron yield [48, 49]. Given that the operational temperature of space antennas and solar panels ranges between about -100°C and 100°C [50], temperature may significantly alter the secondary electron flux magnitude during the potential sensing process. However, this does not affect the spatial distribution of secondary electrons or the detectability of the target, which are the primary variables of interest for this work. The electron beam is, by itself, another heat source. In the experimental setup presented in Sec. III.A, a ~0.01 W electron beam is directed toward an aluminum electrode with an emissivity of ~0.1 and a surface area of ~ 500 cm^2, resulting in a temperature variation of less of 1 K under the black body assumption. Thus, the electron-beam-induced temperature increase can be neglected in the experiments.

III. Materials and methods

A. Experimental setup

The experimental vacuum chamber setup pictured in Fig. 2 is employed to study the observability of secondary electrons in complex differentially-charged targets. It is composed of a 70×70×70 mm^3 spacecraft-like bus electrode and a 145×60 mm^2 panel electrode assembly that is actuated by a stepper engine. Both electrodes together resemble the geometry of a spacecraft and are charged independently up to -800 V by a Matsusada AU-30R1 and a Spellman SL300 high voltage power supply. The assembly is irradiated by a Kimball Physics EMG-4212D electron gun configured to produce an electron beam of 1307 eV and 10 μA. This beam energy value is chosen to maximize the production of secondaries (see Sec. III.B). The resulting flux of x-rays and secondary electrons is measured by an Amptek X123 x-ray spectrometer and a Retarding Potential Analyzer (RPA) that form an angle of ~16° with the electron beam and that stay at least 95 mm away from the tip of the panel electrode. The angular position of the electrode assembly is monitored by means of an incremental rotary high-vacuum Renishaw Tonic encoder.

The experiment is designed to measure the energy spectrum of electrons arriving at the RPA for a given bus and panel electrode potentials and assembly rotation angle. A 3.8 cm diameter Kimball Physics Rugged Phosphor Screen is employed to set the unperturbed electron beam configuration and provide a reference point for the numerical simulation. The beam reaches both electrodes with a ~2.5 cm final beam diameter. Secondary electrons are thus generated over both surfaces, enabling the study of differential charging problems. Further details on the ECLIPS Space Environments Simulation Facility can be found in Ref. [27].

A key difference between the setup represented in Fig. 1 and an actual spacecraft charging scenario is the existence of a grounded vacuum chamber wall (essentially, a Faraday cage) around the experiment. Its presence disturbs the electrostatic potential around the electrodes, and must be taken into account in the definition of the numerical simulation

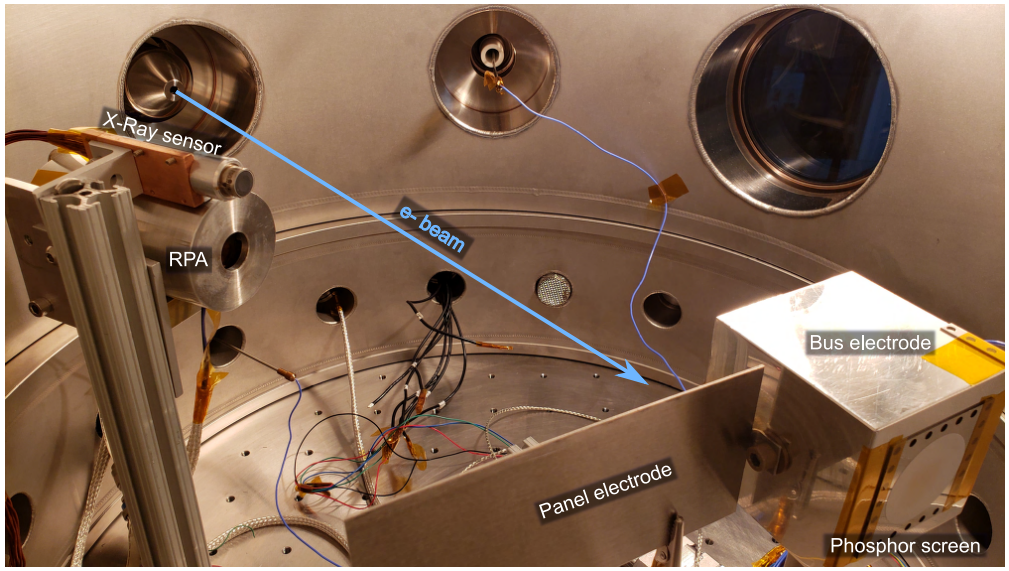

Fig. 2 Experimental setup

framework. Furthermore, the small scale of the experiment makes results particularly sensitive to geometrical and beam pointing errors.

B. Material Properties

The electrodes are made of aluminum, which is characterized by the values $E_{\max} \approx 300$ eV, $\delta_{\max} \approx 0.97$ [26], and $\varphi \approx 4$ eV [38]. As previously noted, these estimations depend strongly on surface conditions that are usually characterized in a laboratory environment [30–33] but hard to estimate in space, and should thus be taken as a rough estimate. This difficulty does not prevent the numerical model from being applied to active spacecraft charging scenarios, because it is in the angular dependence of the result and not in their absolute value where most of the technical interest lies.

Figure 3 represents the secondary electron yield as a function of the energy of a normal incident primary electron (Sec. II.B.1), the angular yield ratio as a function of the angle and incidence of the primary electron (Sec. II.B.2), and the PDF of secondary electron energies (Sec. II.B.4). These relations are implemented in the Lua library of the SIMION model and motivate the selection of an electron beam of ~1300 eV to irradiate the target with a landing energy close to the yield peak.

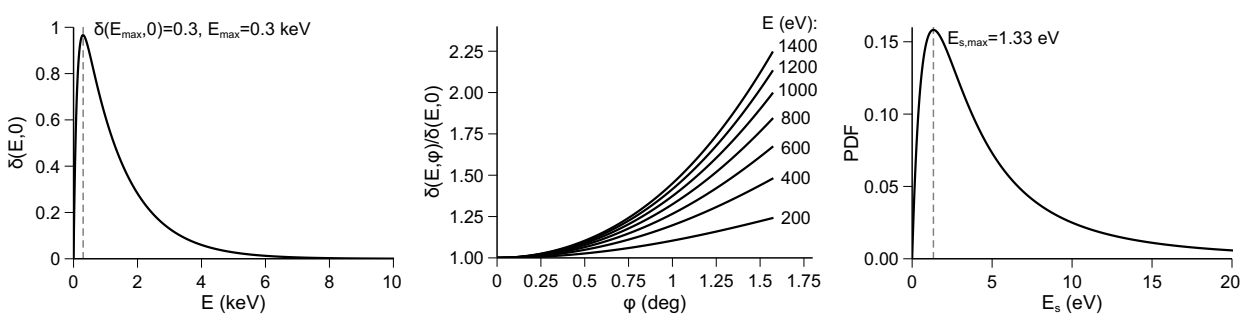

(a) Yield **(b) Angular yield ratio** **(c) Energy distribution**

Fig. 3 Estimated secondary emission properties of aluminum

C. Measurement of secondary electron flux

The flux and spectrum of the secondaries generated over the electrodes is measured using an in-house RPA [46]. The RPA features an entrance grid at ground potential, and a second discriminating grid controlled by a Matsusada AU-30R1 high-voltage power supply. A Keithley DMM6500 multimeter is connected to the grid to measure its voltage and correct the small bias induced by the source. After the grids, a Faraday cup connected to a Keithley 2401 SourceMeter picoammeter is employed to measure the current flux at different energy levels. Electron currents of at least 10 pA with energies up to 1000 eV can be detected with this configuration. Based on previous measurements [20], the RPA efficiency is estimated to be a 20%, although this value should be expected to vary with the direction and intensity of the incoming flux of electrons. For simplicity, a 0.2 correction factor is considered in all simulations.

The RPA is operated in two distinctive modes. In the first, the cumulative secondary electron energy spectrum is obtained by sweeping energy levels from -150 V below the minimum applied potential up to 150 V above the maximum with steps of 1 V and taking the average of 45 samples. The resulting curve is then differentiated to obtain the energy spectrum, as done in Sec. IV.C. In the second mode, the total current is measured at ± 50 eV of the expected energy peak. Both values are subtracted to determine the flux of electrons associated with that energy band. Although this approach provides less information on the population of electrons, it is much faster than the former and eases angular dependence studies like those presented in Sec. IV.D. Both methods are applied in an identical way in SIMION.

D. Particularization of SIMION model

The SIMION simulation framework introduced in Sec. II is tailored, without any loss of generality, for the assembly presented in Fig. 2. A single geometry file (`.gem`) is used to implement the setup described in Sec. III.A, resulting in the 301×301×301 mesh (2 mm/grid unit) depicted in Fig. 4. Each point of the domain requires about 10 bytes of RAM, and up to 20 billion points can be simulated. The floor, walls, main structural supports, and RPA casing are grounded, while the bus and panel electrodes are modeled as fast arrays with adjustable potentials. From a numerical perspective, the walls of the chamber impose a Dirichlet external boundary condition to the Laplace equation (see Sec. II.A).

Because SIMION employs a Cartesian mesh, curved geometries introduce jags that may distort the local electric field and even prevent secondaries from escaping the surface. This problem is overcome by rotating the system while leaving the electrodes aligned with the axes of the model[†]. Previous implementations by the main SIMION programmer,

[†] As the old saying says, "If the hill will not come to Mahomet, Mahomet wil go to the hill" (Francis Bacon, Essays, 1625)

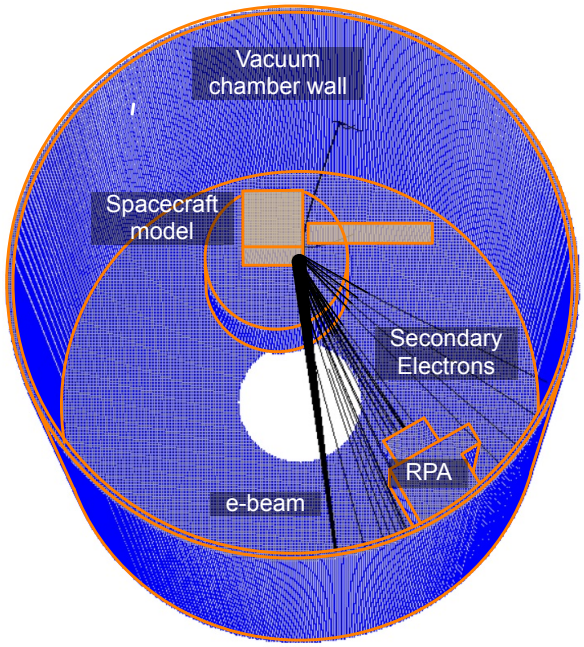

Fig. 4 SIMION model geometry

David Manura, integrate the trajectories of secondary electrons to displace the source region a few units away from the surface (see footnote at the bottom of page 3). That approach is particularly effective for generic geometries and is kept in the Lua libraries of the model for future use.

The determination of surface normal vectors is a critical step for several processes involved in the generation of secondaries, from the imposition of a Lambertian angular distribution to the proper quantification of the secondary electron yield. In this work, the different directions are determined analytically after identifying the impact location of the primary electron. However, it is also possible to estimate the surface normals by taking advantage of the fact that the electric field *should* be orthogonal to the surface. The reasons why this may not always be the case are (i) the inherent numerical errors associated with the computation of ∇V, and (ii) the presence of jags in curved geometries. These issues may be partially corrected if the gradient is computed a few units away from the surface, but the accuracy of the results is strongly dependent on the geometry and electrostatic environment under study. Analytical solutions are consequently implemented in this work.

Matlab is employed to configure and launch the SIMION simulation and also to analyze its outcomes. The SIMION model exports a text file with the kinetic energy of the electrons that reach the interior of the RPA. The collision is detected using SIMION's `segment.terminate()` function, from where the final position of the electron is extracted. If the position is within the RPA detector volume, the energy of the incoming electron is recorded for future analysis.

The new physical processes implemented in the model have been verified by comparing the numerical outcomes with the analytical results given in Sec. II. In order to guarantee the stability of the solution, the electrostatic field is set to converge with a relative error of 10^{-4}, while the electron trajectories are integrated using a fourth order Runge-Kutta method with a maximum step size of one grid unit and a trajectory quality factor of 3 (see Ref. [28] for further details on this parameter). The secondary electron current flux resulting from this configuration varies less than a 5% with respect to equivalent high-fidelity simulations showing virtually no changes in the energy spectrum.

IV. Results and discussion

The experiment pictured in Fig. 2 is tested at the ECLIPS Space Environments Simulation Facility [27] to validate the numerical simulation framework introduced in Sec. II. Numerical and experimental results are presented in this section to understand the detection process and assess the validity of the SIMION model, extracting relevant conclusions for future applications.

A. Overview of electron trajectories

Although charged particles and optical systems are usually considered analogous, the former, unlike the latter, cannot be directly observed. Tracing particle simulation frameworks help overcome this issue with trajectory visualization tools, offering key insights into the behavior of the system.

The trajectories of 100 randomly sampled electron beam particles are represented in Fig. 5 for electrode rotation angles between $-40°$ and $80°$ with respect to the beam axis and a common electrode potential of -800 V. As explained in Sec. III.D, the rotation of the electrode assembly is applied to the rest of the model, keeping the electrodes aligned with the geometrical axes to avoid jags in the surfaces where secondaries are generated. Three clear regimes of operation can be observed: (i) the beam is deflected before reaching the target ($\alpha = -40°, 0°$), (ii) the beam reaches the target, but

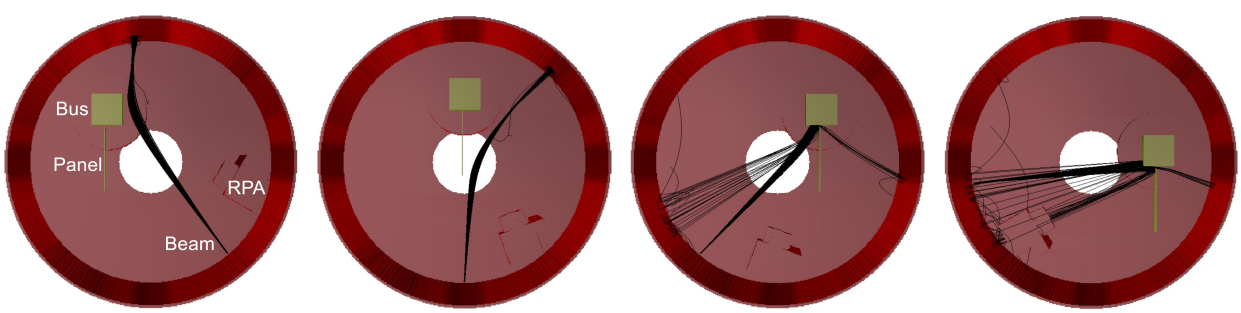

(a) $-40°$ **(b)** $0°$ **(c)** $40°$ **(d)** $80°$

Fig. 5 Electron beam trajectory for different electrode heading angles α

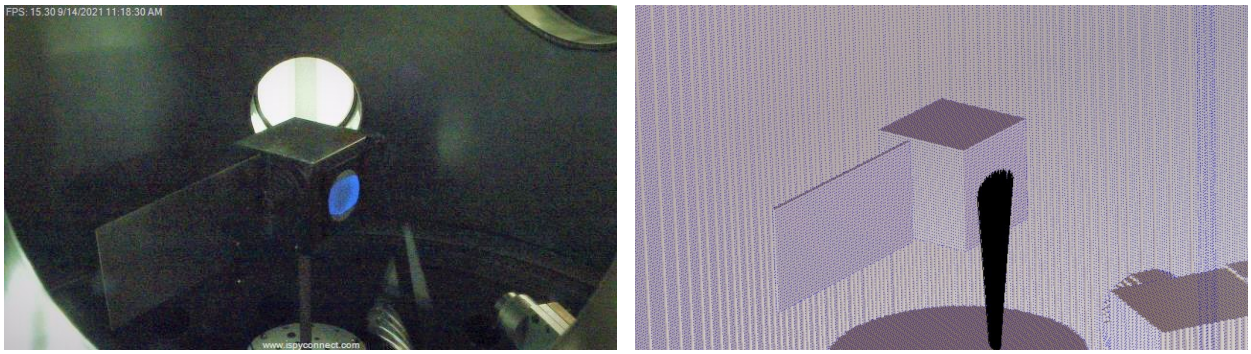

(a) Experiment **(b) SIMION model**

Fig. 6 Centering and calibration of the electron beam

the resulting secondaries do not reach the detector ($\alpha = 40°$), and (iii) the beam reaches the target and the resulting electrons do reach the detector ($\alpha = 80°$). The same focusing effect that has been characterized in previous works [19] is present in the corner between the panel and the bus, concentrating the trajectories of the secondaries and restricting their detectability to narrow regions. It is interesting to note that some trajectories result in more than one secondary electron, and some of them are also sources of second-generation particles. If generated at grounded surfaces, those particles do no have a particular interest for the detection of the electrode potentials because they arrive to the RPA with very small energies. However, in the differential charging scenario, some of those second-generation particles may be created over the surface of the electrode with the highest potential, therefore affecting the detection process. The generation of secondaries over grounded surfaces is thus forbidden in the model in order to improve its computational efficiency.

B. Calibration

A small divergence in the geometrical or electrostatic parameters of the model with respect to the experiment can result in qualitatively different results. This is due, among other factors, to the small scale of the system under study. Even though the SIMION geometry carefully resembles the experimental setup, the vacuum chamber environment does not facilitate taking measurements and some errors are almost unavoidable. In particular, the steering and expansion of the electron beam determine the *effective emission area* of secondary electrons. The beam configuration is thus centered by observing its footprint over the phosphor screen with an electrode heading of $-40°$. The SIMION beam particles configuration file (`.fly2`) is then tuned manually to achieve the matching exemplified in Fig. 6.

C. Complex shapes

The first set of experiments focuses on the detectability of the spacecraft-like assembly when both electrodes are charged to the same potential. This is the most representative case for modern spacecraft, whose external surfaces are generally designed to remain grounded [18, 21]. In order to reduce the uncertainty of the measurements, both electrodes are connected to the Spellman SL300 high voltage power source, whose potential is set and verified manually before each run. The electron gun is operated at 1307 eV, 10 μA, and centered as shown in Fig. 6.

Figure 7 shows the electron distribution measured by the RPA and predicted by the model for rotation angles from $-30°$ to 80° and electrode potentials from -600 V to -800 V. The secondary electron signal is detected only at 70° and 80° for both the model and the experiments, and hence the $-30°$ to 50° data is removed from the plots, leaving the 60° case as a reference. In spite of the presence of numerous sources of uncertainty, the model is able to predict the location and intensity of the peaks with remarkable accuracy. The relative magnitude of the 70° measurements with respect to their 80° counterparts is captured as well. Still, a constant bias of ~20 V is observed in the experiments with respect to the electrode potential. Furthermore, the experimental peaks are almost symmetric, a feature that is not reproduced by SIMION and that is not considered in the physical model described in Sec. II.

Since the same multimeter is used to set the electrode potential and measure the RPA grid voltage, a significant bias in the detection process should be discarded. There are, however, two additional sources of errors that may explain the peak shift and its unexpected symmetry. The first is the presence of oxide or contamination over the electrodes. Previous research has shown that this thin layer can induce spatially inhomogeneous surface potential losses of the order

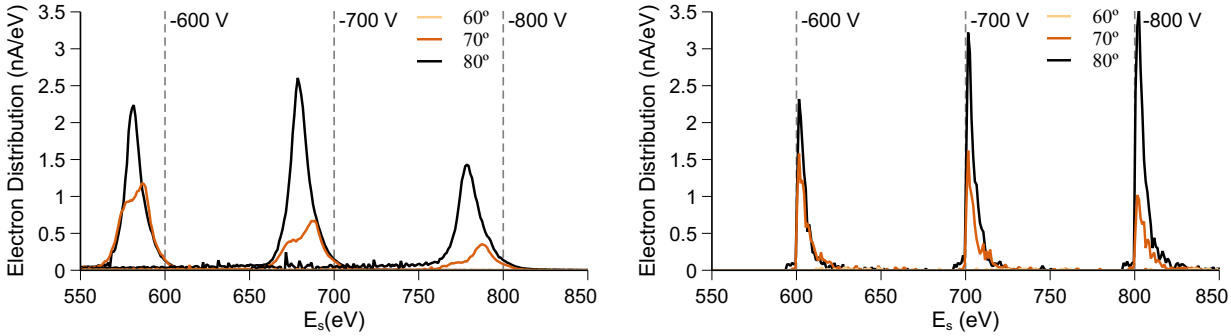

(a) Experimental **(b) SIMION model**

Fig. 7 Secondary electrons spectrum for a range of electrode potentials and rotation angles

of a few volts [31]. The second refers to the performance of the RPA itself, whose internal configuration may result in an apparent plasma heating and a wider energy distributions than reality. Although interesting from a purely scientific viewpoint, these errors do not represent a concern for the applications here considered. In particular, a robust RPA calibration process will likely solve most of these problems, limiting the detection error to tens of volts.

From a technical perspective, the ability of the model to predict the electron flux magnitude is not as relevant as its capacity to determine the orientations for which secondary electrons can be detected. It is clear from Fig. 7 that this primary objective is achieved and that, if an educated estimate of the target surface properties is available, the incoming flux can be reasonably approximated.

D. Differential charging

The differential charging scenario is characterized by a complex potential field in the close proximity of the charged object. Unlike the homogeneous case discussed in the previous section, a potential hill appears between the electrodes (see Chapter 6 in Ref. 26), which due to Eq. 1 and noting the negative charge of the electrons may result in an overall attractive force and a well-localized electron trap [19]. The effect is shown in Fig. 8b, where most of the secondaries are not able to get out of the panel surface in the presence of a 200 V potential difference. As a consequence, the steering and expansion of the electron beam determine the effective emission area, that can vary significantly with small pointing errors. In order to mitigate this effect and reduce the uncertainty of the experimental setup, a wide 3° half-angle electron

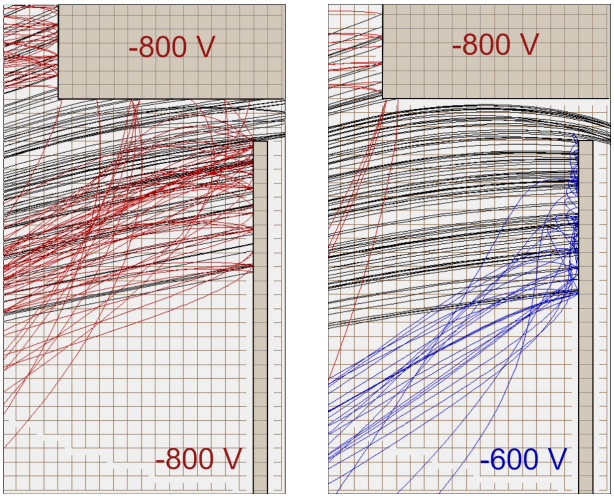

(a) Equipotential surface **(b) Secondary electron trap**

Fig. 8 Secondary electron trajectories between the electrodes

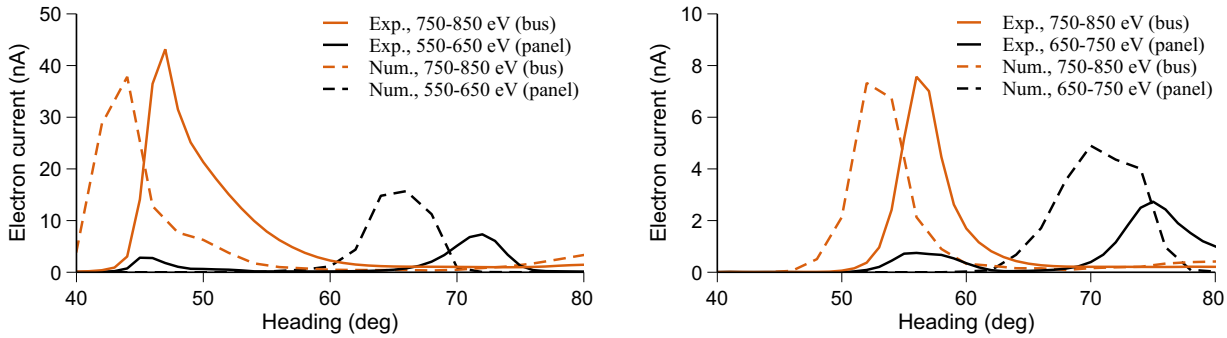

(a) Panel at -600 V, Bus at -800 V **(b) Panel at -700 V, Bus at -800 V**

Fig. 9 Electron current fluxes at selected energy levels

beam at 1307 eV and 10 μA is subsequently employed with the same pointing configuration as before. Future spacecraft systems may adopt the same approach when differential charging is suspected.

Figure 9 shows the experimental and numerical electron current fluxes from a range of secondary electron energies as a function of the electrode assembly heading and charging state. The bus is set to -800 V, while the -600 V and -700 V panel potentials are explored. The secondary electron energy range is chosen to match the potentials of the electrodes within a band of ±50 eV (see Sec. III.C). Experimental results are in good agreement with the simulation, but shifted by a constant ~3° in each case. The independence of this value with the applied electrode potential points to the accumulation of errors in the transcription of the experimental geometry to the SIMION model. Such errors are always hard to avoid in a vacuum chamber experiment, where access is complicated, but do not represent a major technical concern. It is also important to note how, for the first peak, both potentials can be easily determined. This contrasts with the difficulties experienced by the x-ray method in the determination of multiple potentials [51].

More interesting is, however, the absence of a signal from the panel between 40° and 60° in the simulations and the relatively large peak magnitude errors in the 70°-80° range. To shed light on this issue, Fig. 10 depicts the secondary electron trajectories for several heading angles and both potential combinations. Electrons reaching the RPA come from the south face of the bus in the 45° and 55° cases, while secondaries generated at the root of the panel are easily

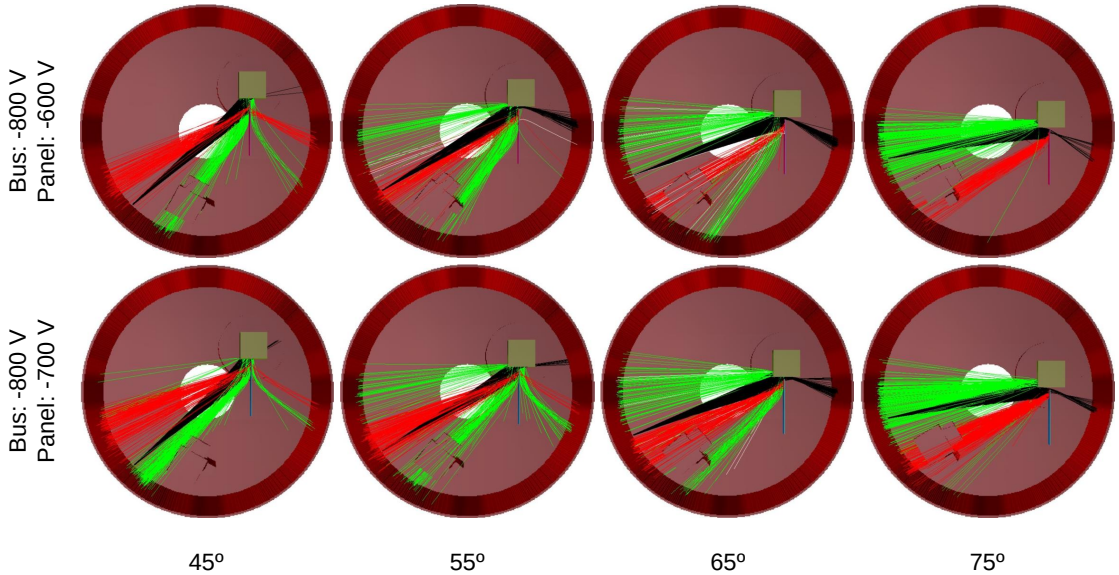

Fig. 10 Electron trajectories from panel (red) and bus (green) electrodes for different heading angles and potential configurations

deflected. Since both electrodes generate particles with very similar energy distributions, it can be readily concluded that the experimental signal from the panel should come from a region close to the bus. A careful examination of the setup depicted in Fig. 2 shows that there is an unmodeled geometry that satisfies this characteristic: the small support of the panel. The higher current flux in the 65° to 75° experimental peaks is harder to explain, but may be attributed to (i) a higher than expected electron beam density in the intersection with the panel, (ii) a small horizontal deflection error of the beam, or (iii) the presence of the unmodeled panel support.

The discussion on the geometrical disagreements between the model and reality reflects the sensitivity of the secondary-electron-based touchless potential sensing method to apparently insignificant features of the target geometry and electron beam properties in a differential charging scenario. This observation is in agreement with the results reported in Ref. [20], and motivates the development of this model and its application in closed-loop detection algorithms.

E. Target observability

The observability space of the experimental setup is explored numerically in Fig. 11 for electrode potentials ranging from -500 V to -800 V, heading angles from 0° to 80°, and the electron beam configuration employed in Sec. IV.D. The incoming electron current is quantified for each electrode energy range as described in Sec. III.C. Not surprisingly, the observable states conform a small subset of the search space, restricted mostly to the 50° to 80° range. Equipotential surfaces are generally easier to observe, as they avoid the generation of electron traps between the electrodes, increasing the effective secondary emission area. It is also important to note that, for those cases where the equipotential state is observable (60° to 80°), the current (or, equivalently, the trajectories of the secondaries) becomes remarkably stable with the applied voltage. Since secondary electrons are created with small initial energies (see Fig. 3c), the beginning of their trajectories closely follows the electrostatic field lines, which determine their future evolution far away from the assembly. Thus, for a sufficiently large electrode potential, the resulting trajectories and measured current will behave as noted.

An interesting feature is also observed for a heading of 10°, where the observability of the panel seems almost independent of the applied potentials. This is just a consequence of the intersection between the electron beam and the tip of the plate, that results in a direct flux of secondaries moving toward the RPA. The effect is overestimated in the SIMION framework due to the relatively coarse Cartesian grid of the model (2 mm/grid unit), which assigns a thickness to the panel of about 4 times the real value.

F. Source regions and sensing strategy

In the analysis carried out in the previous section, a given geometrical and electrostatic configuration is assumed to compute the incoming flux of secondary electrons. Although this approach provides useful information on the coupled dynamics of the active sensing problem, its computational cost is prohibitive for most applications. Instead, future missions are likely to apply a different strategy: (i) determine the *source regions*, defined as the areas of the target where electrons detected at the RPA are generated, and (ii) aim the electron beam at such region. Particle tracing simulation frameworks like the one here introduced can implement this approach and its associated control algorithms. As an example, Fig. 12 shows the source regions for an 80° heading angle and an homogeneous electrode potential to -800 V. The electron beam should be aimed at the green points in order to detect a signal and measure the target properties.

Because the potential distribution of a target spacecraft is unknown beforehand, the determination of source regions is complicated in the initial stages of the sensing process. Qualitative diagnostic information would be helpful to bound the solution space and discover, for instance, if a particular component of the target is electrically detached from the structure. Broad electron beams like the one implemented in Sec. IV.D may be used to excite large portions of the target surface, enabling the measurement of multiple potentials and overcoming electron traps. x-rays-sensing [2], however, is independent from the electrostatic environment and exhibits optimum observability properties [51], which makes it appropriate for diagnostic purposes. However, it also leads to larger potential errors than secondary-electron sensing [**?**]. A combination of both methods is thus ideal to achieve a robust and accurate detection, as highlighted by previous studies [20**?**].

V. Conclusions

This work explores the use of the secondary electron method to detect the electrostatic potential of a charged spacecraft-like electrode assembly. Both the homogeneous and differential charging scenarios are studied. A SIMION-based particle tracing framework that couples the electron beam dynamics and the generation of secondaries is

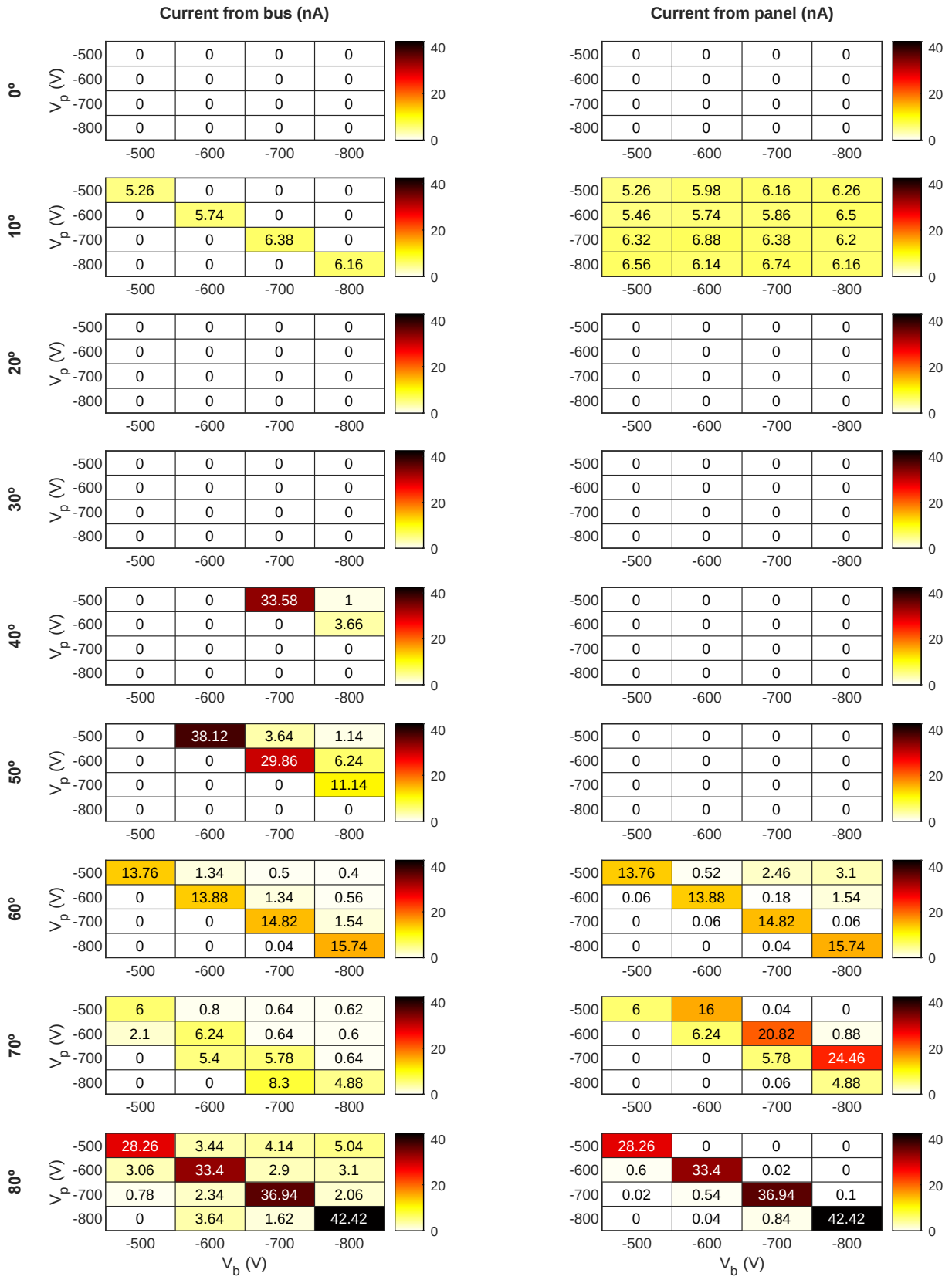

Fig. 11 Observability matrix of the system for different heading angles and panel-bus potentials

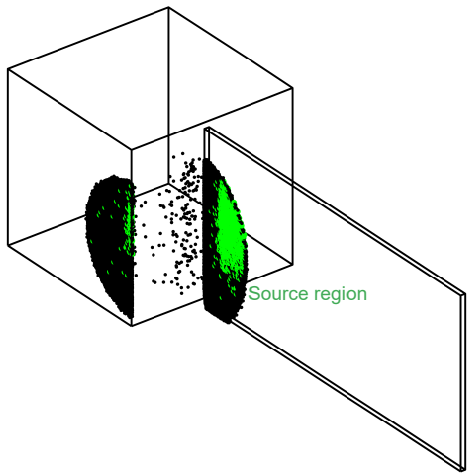

Fig. 12 Source region of secondary electrons reaching the RPA for a heading of $80°$ and an electrode potential of -800 V

implemented and validated, enabling a high-fidelity representation of the problem and providing useful diagnostic tools.

Experiments and numerical simulations show that the flux of secondaries can only be detected in well-defined regions surrounding the target. However, once the detector is within those regions, the potentials are determined with very high accuracy for both the homogeneous and differential charging scenarios. Although the homogeneous case leads to electron trajectories that are very stable with the target potential, differential charging may induce secondary electron traps that can potentially reduce the effective emissive area of the target. It is in this context where accurate particle tracing simulations are needed to model the system and determine the source regions of secondary electrons reaching the detector. Closed-loop potential sensing control algorithms may be developed in the future in combination with existing x-ray sensing methods to address the uncertainties in the initial steps of the detection process and fully exploit the physics of the problem.

Acknowledgments

This work was supported by U.S. Air Force Office of Scientific Research under grant FA9550-20-1-0025, the *La Caixa* Foundation (ID 100010434), under agreement LCF/BQ/AA18/11680099, and the Rafael del Pino Foundation. The authors thank Dr. Kieran Wilson for his support on the setup and operation of the vacuum chamber experiment, Dr. Miles Bengtson for fruitful discussions on the geometrical complexities of the active potential sensing problem, and Mr. David Manura (Adaptas Solutions LLC) for his assistance on the development of the SIMION simulation framework.

References

[1] Bengtson, M. T., Wilson, K. T., and Schaub, H., "Experimental Results of Electron Method for Remote Spacecraft Charge Sensing," *Space Weather*, Vol. 18, No. 3, 2020, pp. 1–12. https://doi.org/10.1029/2019SW002341.

[2] Wilson, K., and Schaub, H., "X-Ray Spectroscopy for Electrostatic Potential and Material Determination of Space Objects," *IEEE Transactions on Plasma Science*, Vol. 47, No. 8, 2019, pp. 3858–3866. https://doi.org/10.1109/TPS.2019.2910576.

[3] Wilson, K. T., Bengtson, M. T., and Schaub, H., "X-ray Spectroscopic Determination of Electrostatic Potential and Material Composition for Spacecraft: Experimental Results," *Space Weather*, Vol. 18, No. 4, 2020, pp. 1–10. https://doi.org/10.1029/2019SW002342.

[4] Bengtson, M., Hughes, J., and Schaub, H., "Prospects and Challenges for Touchless Sensing of Spacecraft Electrostatic Potential Using Electrons," *IEEE Transactions on Plasma Science*, Vol. 47, No. 8, 2019, pp. 3673–3681. https://doi.org/10.1109/TPS.2019.2912057.

[5] Casale, F., Schaub, H., and Biggs, J. D., "Lyapunov Optimal Touchless Electrostatic Detumbling of Geostationary Debris Using Surface Multisphere Models," *AIAA Journal of Spacecraft and Rockets*, Vol. 58, No. 3, 2021. https://doi.org/10.2514/1.A34787.

[6] Hughes, J., and Schaub, H., "Prospects of Using a Pulsed Electrostatic Tractor With Nominal Geosynchronous Conditions," *IEEE Transactions on Plasma Science*, Vol. 45, No. 8, 2017, pp. 1887–1897. https://doi.org/10.1109/TPS.2017.2684621.

[7] Bengtson, M., Wilson, K., Hughes, J., and Schaub, H., "Survey of the electrostatic tractor research for reorbiting passive GEO space objects," *Astrodynamics*, Vol. 2, No. 4, 2018, pp. 291–305. https://doi.org/10.1007/s42064-018-0030-0.

[8] Hughes, J. A., and Schaub, H., "Electrostatic Tractor Analysis Using a Measured Flux Model," *Journal of Spacecraft and Rockets*, Vol. 57, No. 2, 2020, pp. 207–216. https://doi.org/10.2514/1.A34359.

[9] Hammerl, J., and Schaub, H., "Effects of Electric Potential Uncertainty on Electrostatic Tractor Relative Motion Control Equilibria," *Journal of Spacecraft and Rockets*, 2021. https://doi.org/10.2514/1.A35165, *in press*.

[10] Schaub, H., Parker, G. G., and King, L. B., "Challenges and Prospects of Coulomb Spacecraft Formation Control," *The Journal of the Astronautical Sciences*, Vol. 52, No. 1, 2004, pp. 169–193. https://doi.org/10.1007/BF03546427.

[11] Parker, G. G., Schaub, H., Natarajan, A., and King, L. B., "Coulomb Force Virtual Space Structures," *Acta Futura*, Vol. 2, No. ACT-PUB-AFO502, 2006, pp. 39–44. https://doi.org/10.2420/ACT-BOK-AF02.

[12] Stiles, L. A., Schaub, H., Maute, K. K., and Moorer, D. F., "Electrostatically inflated gossamer space structure voltage requirements due to orbital perturbations," *Acta Astronautica*, Vol. 84, 2013, pp. 109–121. https://doi.org/10.1016/j.actaastro.2012.11.007.

[13] Wilson, K., and Schaub, H., "Constrained guidance for spacecraft proximity operations under electrostatic perturbations," *Proceedings of the IEEE Aerospace Engineering Conference, Big Sky, Montana*, 2021. https://doi.org/10.1109/AERO50100.2021.9438194.

[14] Wilson, K. T. H., Bengtson, M., and Schaub, H., "Hybrid Method of Remote Sensing of Electrostatic Potential for Proximity Operations," *IEEE Aerospace Engineering Conference, Big Sky, MO*, 2020. https://doi.org/10.1109/AERO47225.2020.9172772.

[15] Parker, L. W., and Whipple Jr., E. C., "Theory of spacecraft sheath structure, potential, and velocity effects on ion measurements by traps and mass spectrometers," *Journal of Geophysical Research (1896-1977)*, Vol. 75, No. 25, 1970, pp. 4720–4733. https://doi.org/10.1029/JA075i025p04720.

[16] Scime, E. E., Phillips, J. L., and Bame, S. J., "Effects of spacecraft potential on three-dimensional electron measurements in the solar wind," *Journal of Geophysical Research: Space Physics*, Vol. 99, No. A8, 1994, pp. 14769–14776. https://doi.org/10.1029/94JA00489.

[17] Miyake, Y., Cully, C. M., Usui, H., and Nakashima, H., "Plasma particle simulations of wake formation behind a spacecraft with thin wire booms," *Journal of Geophysical Research: Space Physics*, Vol. 118, No. 9, 2013, pp. 5681–5694. https://doi.org/10.1002/jgra.50543.

[18] Barrie, A. C., Cipriani, F., Escoubet, C. P., Toledo-Redondo, S., Nakamura, R., Torkar, K., Sternovsky, Z., Elkington, S., Gershman, D., Giles, B., and Schiff, C., "Characterizing spacecraft potential effects on measured particle trajectories," *Physics of Plasmas*, Vol. 26, No. 10, 2019, p. 103504. https://doi.org/10.1063/1.5119344.

[19] Bengtson, M. T., and Schaub, H., "Electron-Based Touchless Potential Sensing of Shape Primitives and Differentially-Charged Spacecraft," *Journal of Spacecraft and Rockets*, Vol. 0, No. 0, 2021, pp. 1–11. https://doi.org/10.2514/1.A35086.

[20] Romero-Calvo, A., Cano-Gómez, G., and Schaub, H., "Simulation and uncertainty quantification of electron beams in active spacecraft charging scenarios," *Journal of Spacecraft and Rockets*, 2021. *in press*.

[21] Garrett, H. B., and Whittlesey, A. C., "Spacecraft Design Guidelines," *Guide to Mitigating Spacecraft Charging Effects*, John Wiley & Sons, Ltd, 2012, Chap. 3, pp. 26–61. https://doi.org/10.1002/9781118241400.ch3.

[22] Olsen, R. C., McIlwain, C. E., and Whipple Jr., E. C., "Observations of differential charging effects on ATS 6," *Journal of Geophysical Research: Space Physics*, Vol. 86, No. A8, 1981, pp. 6809–6819. https://doi.org/10.1029/JA086iA08p06809.

[23] Grard, R., Knott, K., and Pedersen, "Spacecraft charging effects," *Space Science Reviews*, Vol. 34, No. 3, 1983, pp. 289–304. https://doi.org/10.1007/BF00175284.

[24] Roeder, J. L., and Fennell, J. F., "Differential Charging of Satellite Surface Materials," *IEEE Transactions on Plasma Science*, Vol. 37, No. 1, 2009, pp. 281–289. https://doi.org/10.1109/TPS.2008.2004765.

[25] Ferguson, D., White, S., Rast, R., and Holeman, E., "The Case for Global Positioning System Arcing and High Satellite Arc Rates," *IEEE Transactions on Plasma Science*, Vol. 47, No. 8, 2019, pp. 3834–3841. https://doi.org/10.1109/TPS.2019.2922556.

[26] Lai, S. T., *Fundamentals of Spacecraft Charging: Spacecraft Interactions with Space Plasmas*, Princeton University Press, 2012.

[27] Wilson, K., Bengtson, M., Romero-Calvo, A., Maxwell, J., and Schaub, H., "Characterization of the ECLIPS Space Environments Simulation Facility," *Proceedings of the 2021 AIAA SciTech Forum and Exposition*, 2021. https://doi.org/10.2514/6.2021-1538.

[28] Manura, D., and Dahl, D., *SIMION (R) 8.1 User Manual, Rev-5*, Adaptas Solutions, LLC, Palmer, MA 01069, 2008. URL http://simion.com/manual/.

[29] Sanders, N. L., and Inouye, G. T., "Secondary emission effects on spacecraft charging: Energy distribution considerations," *Spacecraft Charging Technology*, 1978, pp. 747–755. NASA-2071, ADA-084626.

[30] Baglin, V., Bojko, J., Gröbner, O., Henrist, B., Hilleret, N., Scheuerlein, C., and Taborelli, M., "The secondary electron yield of technical materials and its variation with surface treatments," *Proceedings of EPAC 2000, Vienna, Austria*, 2000.

[31] Robertson, S., Sternovsky, Z., and Walch, B., "Reduction of asymmetry transport in the annular Penning trap," *Physics of Plasmas*, Vol. 11, No. 5, 2004, pp. 1753–1756. https://doi.org/10.1063/1.1688337.

[32] Jin, C., Ottaviano, A., and Raitses, Y., "Secondary electron emission yield from high aspect ratio carbon velvet surfaces," *Journal of Applied Physics*, Vol. 122, No. 17, 2017, p. 173301. https://doi.org/10.1063/1.4993979.

[33] Reyes, J. A., Fulford, K. W., Plis, E. A., Hoffmann, R. C., Murray, V. J., Cowardin, H. M., Cone, D., Ferguson, D. C., Bengtson, M. T., Shah, J. R., and Engelhart, D. P., "Spectroscopic behavior of various materials in a GEO simulated environment," *Acta Astronautica*, Vol. 189, 2021, pp. 576–583. https://doi.org/10.1016/j.actaastro.2021.09.014.

[34] Knuth, D., *The Art of Computer Programming*, Vol. 1-3, Addison-Wesley Longman Publishing Co., Inc., Boston, MA, USA, 1998.

[35] Darlington, E. H., and Cosslett, V. E., "Backscattering of 0.5-10 keV electrons from solid targets," *Journal of Physics D: Applied Physics*, Vol. 5, No. 11, 1972, pp. 1969–1981. https://doi.org/10.1088/0022-3727/5/11/305.

[36] Bruining, H., *Physics and Applications of Secondary Electron Emission*, New York: McGraw-Hill Book Co., Inc. London: Pergamon Press Ltd., 1954. Chapter 7: Theory of Secondary Electron Emission; Discussion of Some Properties of Secondary Electrons.

[37] Greenwood, J., "The correct and incorrect generation of a cosine distribution of scattered particles for Monte-Carlo modelling of vacuum systems," *Vacuum*, Vol. 67, No. 2, 2002, pp. 217–222. https://doi.org/10.1016/S0042-207X(02)00173-2.

[38] Chung, M. S., and Everhart, T. E., "Simple calculation of energy distribution of low-energy secondary electrons emitted from metals under electron bombardment," *Journal of Applied Physics*, Vol. 45, No. 2, 1974, pp. 707–709. https://doi.org/10.1063/1.1663306.

[39] Fahr, Hans J., and Heyl, M., "Debye screening under non-equilibrium plasma conditions," *Astronomy & Astrophysics*, Vol. 589, 2016, p. A85. https://doi.org/10.1051/0004-6361/201628082.

[40] Seubert, C. R., Stiles, L. A., and Schaub, H., "Effective Coulomb force modeling for spacecraft in Earth orbit plasmas," *Advances in Space Research*, Vol. 54, No. 2, 2014, pp. 209–220. https://doi.org/https://doi.org/10.1016/j.asr.2014.04.005.

[41] Thiébault, B., Hilgers, A., Sasot, E., Laakso, H., Escoubet, P., Génot, V., and Forest, J., "Potential barrier in the electrostatic sheath around a magnetospheric spacecraft," *Journal of Geophysical Research: Space Physics*, Vol. 109, No. A12, 2004. https://doi.org/10.1029/2004JA010398.

[42] Engwall, E., Eriksson, A. I., and Forest, J., "Wake formation behind positively charged spacecraft in flowing tenuous plasmas," *Physics of Plasmas*, Vol. 13, No. 6, 2006, p. 062904. https://doi.org/10.1063/1.2199207.

[43] Ergun, R. E., Malaspina, D. M., Bale, S. D., McFadden, J. P., Larson, D. E., Mozer, F. S., Meyer-Vernet, N., Maksimovic, M., Kellogg, P. J., and Wygant, J. R., "Spacecraft charging and ion wake formation in the near-Sun environment," *Physics of Plasmas*, Vol. 17, No. 7, 2010, p. 072903. https://doi.org/10.1063/1.3457484.

[44] Guillemant, S., Génot, V., Vélez, J.-C. M., Sarrailh, P., Hilgers, A., and Louarn, P., "Simulation Study of Spacecraft Electrostatic Sheath Changes With the Heliocentric Distances From 0.044 to 1 AU," *IEEE Transactions on Plasma Science*, Vol. 41, No. 12, 2013, pp. 3338–3348. https://doi.org/10.1109/TPS.2013.2246193.

[45] Wang, X., Pilewskie, J., Hsu, H.-W., and Horányi, M., "Plasma potential in the sheaths of electron-emitting surfaces in space," *Geophysical Research Letters*, Vol. 43, No. 2, 2016, pp. 525–531. https://doi.org/10.1002/2015GL067175.

[46] Bengtson, M. T., "Electron Method for Touchless Electrostatic Potential Sensing of Neighboring Spacecraft," Ph.D. thesis, University of Colorado Boulder, 2020. URL http://hanspeterschaub.info/Papers/grads/MilesBengtson.pdf.

[47] Seely, S., "Work Function and Temperature," *Phys. Rev.*, Vol. 59, 1941, pp. 75–78. https://doi.org/10.1103/PhysRev.59.75, URL https://link.aps.org/doi/10.1103/PhysRev.59.75.

[48] Pomerantz, M. A., "The Temperature Dependence of Secondary Electron Emission from Oxide-Coated Cathodes," *Phys. Rev.*, Vol. 70, 1946, pp. 33–40. https://doi.org/10.1103/PhysRev.70.33, URL https://link.aps.org/doi/10.1103/PhysRev.70.33.

[49] Zeng, L., Zhou, X., Cheng, R., Wang, X., Ren, J., Lei, Y., Ma, L., Zhao, Y., Zhang, X., and Xu, Z., "Temperature and energy effects on secondary electron emission from SiC ceramics induced by Xe17+ ions," *Scientific Reports*, Vol. 7, No. 1, 2017, p. 6482. https://doi.org/10.1038/s41598-017-06891-9.

[50] Wertz, J., and Larson, W., *Space Mission Analysis and Design*, Space Technology Library, Springer Netherlands, 1999.

[51] Hammerl, J., Romero-Calvo, A., López, A., and Schaub, H., "Touchless potential sensing of complex differentially-charged shapes using X-rays," *Proceedings of the AIAA SciTech 2022 Forum and Exposition*, 2022.